

Microlensing under Shear

Yoon-Hyun Ryu and Myeong-Gu Park

*Department of Astronomy and Atmospheric Sciences, Kyungpook National University,
Daegu 702-701, Korea*

yhryu@knu.ac.kr, mgp@knu.ac.kr

ABSTRACT

Over two thousand Galactic microlensing events have been discovered so far. All of them can be explained by events caused by single or multiple lenses (including binaries and planetary companions). However, when a microlensing event occurs in highly dense star fields such as in the Galactic bulge or in a globular cluster, it is necessarily affected by the shear from the global distribution of mass near the lens star. We investigate the distortions due to this shear in the microlensing light curves and in the astrometric microlensing centroid shift trajectories. As expected, the light curve deviation increases as the shear increases and the impact parameter decreases. Although the light curve in the presence of a small shear is similar to the simple Paczyński curve with a slightly smaller impact parameter, the detailed difference between the light curve with and without shear reflects the direction and the magnitude of the shear. The centroid shift trajectory also deviates from a simple ellipse in the presence of shear. The distortion of the centroid shift trajectory increases as the impact parameter decreases, and the shape of the trajectory becomes complicated when the impact parameter becomes small enough. The magnitude of the maximum distortion depends on the magnitude and the direction of the shear. For a source trajectory in a given direction, the time of the maximum distortion depends mostly on the impact parameter and hardly on the shear. It is possible to determine the magnitude of the shear and its direction if both the time and the magnitude of the maximum astrometric distortion are measured. The magnitude of the shear produced by the Galactic bulge or a globular cluster falls in the range 10^{-6} – 10^{-4} in normalized units. Although the actual determination of the shear from the Galactic sub-structures will not be easy due to complications such as binary companion, future large scale microlensing experiments may enable us to determine the shear in some high amplification events, leading eventually to mapping the Galactic mass distribution.

Subject headings: gravitational lensing — Galaxy: bulge — globular clusters: general

1. Introduction

Since Paczyński (1986; see also Gott 1981) first proposed gravitational microlensing as a tool to detect massive astronomical compact objects (MACHOs) in the Galactic halo, three groups (OGLE, Udalski et al. 1992; EROS, Aubourg et al. 1993; MACHO, Alcock et al. 1993) independently discovered the first microlensing events, and subsequent observations detected by now more than two thousand microlensing events.

Gravitational microlensing has been applied to various fields of astronomy, such as the studies of Galactic structure and stellar populations and the search for extra-solar planets. With increasing potential of microlensing as a versatile astrophysical tool, more advanced microlensing experiments such as highly precise follow-up observations and pixel lensing observations are currently being carried out, and next generation microlensing experiments such as astrometric microlensing observations by using the *Space Interferometry Mission (SIM)* and Keck and VLT interferometers have been proposed.

Microlensing experiments are conducted toward very dense star fields such as the Galactic bulge and the Magellanic clouds. When a microlensing event occurs in these crowded fields, it is necessarily affected by the shear caused by the global distribution of mass around the lens star. Chang & Refsdal (1979, 1984) have discussed the effect of a star on the macro-lensed image produced by the galaxy as a whole, often referred to as the ‘Chang & Refsdal lens’. Their lens model is characterized by ‘convergence’ and ‘shear’: the former depends on the mass density within the beam and determines the magnification of the image, while the latter depends on the mass distribution outside of the beam and determines the distortion of the image (see e.g. Schneider et al. 1992). They pointed out that the configurations and the observational characteristics of macro-lensed images can be significantly affected by a single star. However, their work considered quasar lensing under shear, and focused only on the image configurations. In this paper, we investigate how the shear affects the stellar microlensing light curves and the astrometric centroid shift trajectories.

The paper is organized as follows. We first introduce a single point-mass microlensing in §2 to compare with the point-mass lensing with shear in §3.1. In §3.2 and §3.3, we discuss the distortions in the micro-lensed light curves and centroid shift trajectories in the presence of the shear. In §4, we discuss possible applications to Galactic microlensing experiments.

In §5, we summarize the results and conclude.

2. Single Point Mass Microlensing

Microlensing occurs when a lensing mass passes very close to the line of sight to a background source star. When the lensing mass is a single point mass, the source star splits into two images. The separation between the two images is of the order of the Einstein radius, which is related to the physical parameters of the lens system by

$$\theta_E = \sqrt{\frac{4Gm}{c^2} \frac{D_{ls}}{D_l D_s}}, \quad (1)$$

where m is the mass of the lens, D_l and D_s the distances from the observer to the lens and source, respectively, and D_{ls} the distance from the lens to the source. The angular positions of the images with respect to the lens are

$$\boldsymbol{\theta}_{\pm} = \frac{1}{2} \left(\mathbf{u} \pm \sqrt{u^2 + 4} \frac{\mathbf{u}}{u} \right) \theta_E, \quad (2)$$

where

$$\mathbf{u} = \left(\frac{t - t_0}{t_E} \right) \hat{x} + u_0 \hat{y} \quad (3)$$

is the projected lens-source separation vector in units of the θ_E , u_0 the impact parameter, t_0 the time of maximum amplification. The Einstein ring radius crossing time or the Einstein time scale, t_E , is given by (see e.g. Gould 2000),

$$t_E = \frac{\theta_E}{\mu_{rel}}, \quad (4)$$

where

$$\theta_E = \sqrt{\frac{4Gm}{c^2} \frac{\pi_{rel}}{AU}}, \quad \pi_{rel} = \frac{1}{D_l} - \frac{1}{D_s},$$

π_{rel} and μ_{rel} are the relative source-lens parallax and proper motion, respectively. The magnification of each individual image is given by

$$A_{0,\pm} = \frac{1}{2} \left[\frac{u^2 + 2}{u\sqrt{u^2 + 4}} \pm 1 \right], \quad (5)$$

where $A_{0,+}$ and $A_{0,-}$ are the magnification factors of the major and minor images, respectively. The position of the center of light (centroid) corresponds to the magnification-weighted mean of image positions, i.e.

$$\boldsymbol{\theta}_0 = \frac{A_{0,+}\boldsymbol{\theta}_+ + A_{0,-}\boldsymbol{\theta}_-}{A_0} \quad (6)$$

with $A_0 = A_{0,+} + A_{0,-}$ is the total magnification. The centroid shift $\delta\boldsymbol{\theta}_0$ is defined as the difference between the image centroid $\boldsymbol{\theta}_0$ and the unlensed source position $\boldsymbol{\theta}_{s,0}$, and is related to the lensing parameters by

$$\delta\boldsymbol{\theta}_0 = \boldsymbol{\theta}_0 - \boldsymbol{\theta}_{s,0} = \frac{\theta_E}{u^2 + 2} \mathbf{u} . \quad (7)$$

The position of the centroid shift caused by a single point-mass lensing follows an ellipse (Walker 1995; Jeong, Han & Park 1999), which is represented by

$$\frac{x^2}{a^2} + \frac{y^2}{b^2} = 1 , \quad (8)$$

where the x and y represent the centroid shift parallel and normal to the lens-source transverse motion, respectively. The semi-major axis a and semi-minor axis b depend on the impact parameter u_0 as

$$a = \frac{\theta_E}{2(u_0^2 + 2)^{1/2}} , \quad b = \frac{u_0\theta_E}{2(u_0^2 + 2)} . \quad (9)$$

3. Microlensing under Shear

3.1. Lens Equation

When a source is lensed by a point mass m plus planar mass distribution, the lens equation becomes (see e.g. Schneider et al. 1992; An 2005; An & Evans 2006)

$$\mathbf{s} = \mathbf{r} - \frac{\mathbf{r}}{r^2} - \boldsymbol{\alpha}(\mathbf{r}) , \quad (10)$$

where the two-dimensional vectors \mathbf{r} and \mathbf{s} are the positions of the images and the unlensed source, respectively. The vector \mathbf{r} in the lens (image) plane is normalized by $r_E = \theta_E D_l$ and the vector \mathbf{s} in the source plane by $s_E = \theta_E D_s$. The scaled deflection angle $\boldsymbol{\alpha}(\mathbf{r})$ due to the additional mass distribution in the lens plane is given by the gradient of the deflection potential ψ :

$$\boldsymbol{\alpha}(\mathbf{r}) = \nabla\psi(\mathbf{r}) , \quad (11)$$

where

$$\psi(\mathbf{r}) = \frac{1}{\pi} \int_{R^2} d^2r' \sigma(\mathbf{r}') \ln |\mathbf{r} - \mathbf{r}'| . \quad (12)$$

Here $\sigma(\mathbf{r})$ represents the surface mass density $\Sigma(\mathbf{r})$ normalized by the critical surface mass density Σ_{cr} ,

$$\sigma(\mathbf{r}) = \frac{\Sigma(\mathbf{r})}{\Sigma_{cr}} , \quad \Sigma_{cr} = \frac{c^2 D_s}{4\pi G D_l' D_{l's}} , \quad (13)$$

where D_{ν} is the distance from the observer to the planar mass distribution, which is in general different from D_l , the distance to the point mass m , and similarly for D_{ν_s} .

When the mass distribution consists of a stellar mass and a much larger-scale extended mass distribution, the lens equation is approximated by a point mass plus quadrupole lens model (Chang & Refsdal 1984; see also Kovner 1987),

$$\mathbf{s} = \mathbf{r} - \frac{\mathbf{r}}{r^2} - \begin{pmatrix} \kappa + \gamma & 0 \\ 0 & \kappa - \gamma \end{pmatrix} \mathbf{r}. \quad (14)$$

The quadrupole term is specified by the convergence κ and the shear γ . These quantities are the two-dimensional second derivatives of $\psi(\mathbf{r})$:

$$\kappa = \frac{\psi_{11} + \psi_{22}}{2}, \quad \gamma = \sqrt{\gamma_1 + \gamma_2}, \quad (15)$$

where

$$\gamma_1 = \frac{\psi_{11} - \psi_{22}}{2}, \quad \gamma_2 = \psi_{12} = \psi_{21}, \quad (16)$$

and ψ_{ij} is the partial derivative of $\psi(\mathbf{r})$ with respect to r_i ,

$$\psi_{ij} \equiv \frac{\partial}{\partial r_i} \frac{\partial}{\partial r_j} \psi(\mathbf{r}). \quad (17)$$

If we define the rescaled coordinates \mathbf{S} and \mathbf{R} as

$$\mathbf{S} \equiv \frac{\mathbf{s}}{\sqrt{|1 - \kappa + \gamma|}}, \quad \mathbf{R} \equiv \sqrt{|1 - \kappa + \gamma|} \mathbf{r}, \quad (18)$$

equation (14) becomes

$$\mathbf{S} = \varepsilon \begin{pmatrix} \Lambda & 0 \\ 0 & 1 \end{pmatrix} \mathbf{R} - \frac{\mathbf{R}}{R^2}, \quad (19)$$

where

$$\varepsilon \equiv \text{sign}(1 - \kappa + \gamma), \quad \Lambda \equiv \frac{1 - \tilde{\gamma}}{1 + \tilde{\gamma}}, \quad (20)$$

and the reduced shear $\tilde{\gamma}$ is

$$\tilde{\gamma} \equiv \frac{\gamma}{1 - \kappa}. \quad (21)$$

For convenience, $\tilde{\gamma}$ will be referred simply as the shear henceforth.

In order to solve the lens equation, we introduce the polar coordinates (R, φ) in the lens plane: $R_x \equiv R \cos \varphi$ and $R_y \equiv R \sin \varphi$. Then equation (19) becomes

$$S_x = R(\varepsilon\Lambda - R^{-2}) \cos \varphi, \quad S_y = R(\varepsilon - R^{-2}) \sin \varphi, \quad (22)$$

which yields a fourth-order equation for R^2 (Schneider et al. 1992),

$$\begin{aligned} & \Lambda^2 R^8 - [\varepsilon 2\Lambda(\Lambda + 1) + S_x^2 + \Lambda^2 S_y^2] R^6 \\ & + [\Lambda^2 + 4\Lambda + 1 + \varepsilon 2(S_x^2 + \Lambda S_y^2)] R^4 \\ & - [\varepsilon 2(\Lambda + 1) + S_x^2 + S_y^2] R^2 + 1 = 0, \end{aligned} \quad (23)$$

We solve equation (23) by Laguerre’s method.

3.2. Light Curve

Equation (23) has either zero, two, or four real roots, each of which corresponds to the position of the individual image. The Jacobian matrix of equation (19) is

$$\frac{\partial \mathbf{S}}{\partial \mathbf{R}} = \begin{pmatrix} \varepsilon \Lambda + \frac{R_x^2 - R_y^2}{R^4} & \frac{2R_x R_y}{R^4} \\ \frac{2R_x R_y}{R^4} & \varepsilon 1 - \frac{R_x^2 - R_y^2}{R^4} \end{pmatrix}, \quad (24)$$

whose determinant is

$$\det \left(\frac{\partial \mathbf{S}}{\partial \mathbf{R}} \right) = \frac{1}{R^4} [\Lambda (R_x^2 + R_y^2)^2 + \varepsilon (1 - \Lambda) (R_x^2 - R_y^2) - 1]. \quad (25)$$

The magnification of each individual image is

$$A_{\gamma,i} = \left| \det \left(\frac{\partial \mathbf{s}}{\partial \mathbf{r}} \right) \right|^{-1} = \frac{1}{1 - \kappa + \gamma} \left| \det \left(\frac{\partial \mathbf{S}}{\partial \mathbf{R}} \right) \right|^{-1}. \quad (26)$$

The total magnification is the sum of the magnifications of individual images, $A_\gamma = \sum_i A_{\gamma,i}$. In order to quantify how much the light curve in the presence of shear deviates from that in the absence of shear, we define the excess magnification as

$$\delta A \equiv A_\gamma - A_0, \quad (27)$$

where A_γ and A_0 represent the magnifications with and without shear, respectively. In Figure 1, we present the contour maps of magnification A_γ (left panels) and excess magnification δA (right panels) as a function of source position (s_x, s_y) for $\tilde{\gamma} = 10^{-2}$, 10^{-4} , and 10^{-6} , respectively. The caustics appear as the central diamonds in the left panel of Figure 1, whose full width on the x -axis is $4\gamma(1 - \kappa + \gamma)^{-1/2}$ and that on the y -axis is $4\gamma(1 - \kappa - \gamma)^{-1/2}$ (Han et al. 2005). When the source is outside the caustic, i.e. $u_0 \gtrsim 4\gamma$, the number of images is two as in the simple lensing without shear.

The series solution of equation (23) can be derived under the assumption $\kappa \ll \gamma \ll |\mathbf{s}| \ll 1$. The excess magnification δA is calculated in powers of $\tilde{\gamma}$, and the leading term yields

$$\delta A \simeq \tilde{\gamma} \left(-\frac{1}{2s} + \frac{3s_y^2}{s^3} \right).$$

Although other geometric configurations will yield different values, the order of magnitude of the deviation will be the same, $\delta A \sim \tilde{\gamma}/u_0$. This shows that even very small shear can produce a significant deviation in the light curve if the impact parameter is small enough, that is in high-magnification events.

We now investigate the light curves for typical source trajectories. Since the trajectory of the source does not coincide with the direction of the shear in general, we choose source trajectories with various angles (see Fig. 2). Figure 2 shows the angle ϑ defined as the angle between the x -axis and the source trajectory. The dotted ring around the lens (its position marked by ‘ \times ’) is the Einstein ring. In the left panel of Figure 3, we present the lensing light curves for the corresponding source trajectories marked in Figure 2 with values of the shear $\tilde{\gamma} = 0.01, 0.005, 0.001$, and $\tilde{\gamma} = 0.0$ (no shear). All light curves have the same impact parameter, $u_0 = 0.3$. The minimum magnification A_γ is greater than the minimum of A_0 by a factor $1/(1 + \tilde{\gamma})(1 - \tilde{\gamma})$ for $\tilde{\gamma} < 1$. This is because the brightness of the source is increased by the shear alone even in the absence of the point-mass lens. In the right panel of Figure 3, we present the magnitude and pattern of δA for various shear values and source trajectories. We find that the excess magnification increases as $\tilde{\gamma}$ increases and the excess becomes maximum when the source trajectory is parallel to the shear direction ($\vartheta = 0^\circ$). Even if the light curves have the same shear and the impact parameter, the positions and heights of the peak deviations vary with ϑ . We find that the value of maximum δA decreases as source trajectory becomes perpendicular to the shear direction ($\vartheta = 90^\circ$). We also find that unless the source trajectory is parallel or perpendicular to the shear direction, the deviation δA becomes asymmetric in the presence of the shear.

In real observations of microlensing, however, each light curve will be first fitted by a theoretical microlensing light curve such as the Paczyński curve. So we check how the light variation induced by the presence of shear deviates from the single mass lensing curve. In Paczyński curve, the peak amplification A_p is a simple function of the impact parameter u_0 ,

$$A_p = \left[1 - \left(\frac{u_0^2}{2} + 1 \right)^{-2} \right]^{-1/2}. \quad (28)$$

We compare the light curve in the presence of shear with the Paczyński curve that has the same peak magnification A_p at $t = t_0$ against the background magnification due to the shear alone, $A_\gamma|_{s \rightarrow \infty}$. The impact parameter u_{0p} (eq. [28]) from the fitted Paczyński curve

is always slightly smaller than the true impact parameter u_0 because shear increases the maximum magnification. The detailed shapes of the deviations from the Paczyński curve for various $\tilde{\gamma}$ and ϑ are shown in Figure 4. As expected from the Figure 3, the light curve becomes asymmetric in the presence of the shear when the source trajectory is not parallel or perpendicular to the direction of the shear. By fitting the deviation from Paczyński curve with an appropriate lens model with shear, it is possible, in principle, to determine the magnitude and the direction of the shear if the photometric accuracy is good enough to measure the deviation. In real observations, the light curve as a whole will be fitted by the Paczyński curve, and the shape and the maximum value of the deviation can be somewhat smaller than that from the simple fitting of the maximum amplification.

3.3. Centroid Shift

We define the centroid shift by

$$\delta\boldsymbol{\theta}_\gamma \equiv \boldsymbol{\theta}_\gamma - \boldsymbol{\theta}_s, \quad (29)$$

where

$$\boldsymbol{\theta}_\gamma = \frac{\sum A_{\gamma,i} \mathbf{r}_i}{A_\gamma} \theta_E, \quad \boldsymbol{\theta}_s = \mathbf{s}_\gamma \theta_E, \quad (30)$$

\mathbf{s}_γ is the position of the image that would result from the shear alone in the absence of the point mass, i.e. $\mathbf{s}_\gamma = \mathbf{s} + \boldsymbol{\alpha}(\mathbf{s}_\gamma)$. When microlensing occurs in the presence of shear, astrometric observations will measure $\delta\boldsymbol{\theta}_\gamma$. From equations (18) and (22), we see that

$$\mathbf{s}_{\gamma,x} = \frac{s_x}{1 - \kappa - \gamma}, \quad \mathbf{s}_{\gamma,y} = \frac{s_y}{1 - \kappa + \gamma}, \quad (31)$$

which shows the whole field is sheared even before stellar microlensing occurs. This affects the observed proper motion of the source as well as the estimate of the lensing parameters. If the source proper motion increases by the factor Λ^{-1} , the Einstein ring radius crossing time would change to

$$t'_E = \Lambda t_E. \quad (32)$$

The trajectories of $\delta\boldsymbol{\theta}_\gamma$ in units of θ_E are shown in Figure 5 for given ϑ 's and $\tilde{\gamma}$'s. The left panel shows the change of centroid shift trajectories depending on ϑ and $\tilde{\gamma}$. The centroid shift trajectories (*dotted, dot-dashed, and dashed curves*) deviate from a simple astrometric ellipse (*solid curve*), and both the shape and the magnitude of the distortion vary with ϑ and $\tilde{\gamma}$. The right panel of Figure 5 shows the variation of the centroid shift trajectory depending on the impact parameter u_0 . The trajectories of centroid shift for different u_0 in

the presence of the shear are different from each other. The shape becomes more complex and the distortion increases as u_0 decreases. The distortion becomes very large for small values of u_0 even when the shear is small.

To quantify the deviation of the centroid shift trajectory, we calculate the excess centroid shift defined as

$$\Delta\theta \equiv \delta\theta_\gamma - \delta\theta_0, \quad (33)$$

where $\delta\theta_\gamma$ and $\delta\theta_0$ represent the centroid shifts with and without shear, respectively. The deviation $\Delta\theta$ is really the deviation from the centroid shift ellipse which is expected in a point mass lensing without shear. The trajectories of $\Delta\theta$ are shown in the left panel of Figure 6. The arrow in each panel shows the direction of the centroid motion with the progress of time. All excess centroid shifts have one twist. This is similar to the planet-induced microlensing centroid shift (Han 2002). The magnitude of the excess centroid shift defined as $\Delta\theta \equiv |\delta\theta_\gamma| - |\delta\theta_0|$ is shown in the right panel of Figure 6. We find that major deviation occurs when $-2 < (t - t_0)/t_E < 2$, as expected. The sign of $\Delta\theta$ can be either positive or negative. The detailed shape of $\Delta\theta$ as a function of $(t - t_0)/t_E$ depends on ϑ . For intermediate values of ϑ , e.g., $\vartheta = 30^\circ$ or 60° , $\Delta\theta$ changes its sign near $t = t_0$.

We further investigate the magnitude of the maximum distortion, $\Delta\theta_{max}$, and the time of maximum distortion, t_{max} . Figure 7a shows how $\Delta\theta_{max}$ in units of θ_E varies as a function of $\tilde{\gamma}$ for different values of ϑ and u_0 . For small enough value of $\tilde{\gamma}$, $\log \Delta\theta_{max}$ increases linearly as $\log \tilde{\gamma}$ increases. For a given $\tilde{\gamma}$, $\Delta\theta_{max}$ becomes maximum when $\vartheta = 0^\circ$ and 90° and minimum when $\vartheta = 45^\circ$. Figure 7b shows the dependence of $\Delta\theta_{max}$ on u_0 for given $\tilde{\gamma}$ and $\vartheta = 45^\circ$. Figure 8a and 8b show t_{max} in units of t_E as a function of $\tilde{\gamma}$ for different ϑ and u_0 , which Figure 8c shows the dependence of t_{max} on u_0 . For each ϑ and u_0 , t_{max} is nearly constant, independent of $\tilde{\gamma}$. Since u_0 can be determined from the centroid shift trajectory, $\tilde{\gamma}$ can be determined from the $\Delta\theta_{max}$ (Fig. 7a) and ϑ from t_{max} (Fig. 8a). Therefore, it is possible to determine the shear and its direction if we determine by astrometry both the time t_{max} and the magnitude of the maximum astrometric distortion $\Delta\theta_{max}$. Needless to say, one can always fit the full lensing (with shear) model to each individual case, and determine the shear and its direction.

As in §3.2, we can also calculate the series expressions for $\Delta\theta$ in powers of $\tilde{\gamma}$ under the same assumption:

$$\Delta\theta \simeq \tilde{\gamma} \left[2 \left(\frac{s^2 - 1}{s} \right) + 4s_y^2 \left(\frac{1 - s^2}{s^3} \right) \right] \quad (34)$$

where

$$s = \sqrt{T^2 + u_0^2}, \quad s_y = -T \sin \vartheta + u_0 \cos \vartheta, \quad (35)$$

and

$$T \equiv \left(\frac{t - t_0}{t_E} \right). \quad (36)$$

The time of maximum distortion, t_{max} , is given by a root of the equation

$$T^5 + (4u_0^2 + 1)T^3 + (2u_0^3 + 4u_0) \tan 2\vartheta T^2 + (3u_0^4 - 5u_0^2)T + (2u_0^5 - 2u_0^3) \tan 2\vartheta = 0. \quad (37)$$

This equation has three real roots, and the one with the smallest absolute value corresponds to t_{max} . The angle ϑ is now

$$\vartheta = \frac{1}{2} \arctan \left[\frac{-t_{max}^5 - (4u_0^2 + 1)t_{max}^3 + (5u_0^2 - 3u_0^4)t_{max}}{(2u_0^3 + 4u_0)t_{max}^2 + (2u_0^5 - 2u_0^3)} \right]. \quad (38)$$

Hence, we can also approximately determine $\tilde{\gamma}$ and its direction ϑ from equations (34) and (38) from t_{max} and $\Delta\theta_{max}$.

4. Application to Galactic Microlensing

Now we discuss Galactic microlensing affected by the shear. Consider a microlensing system that consists of a single lensing star under a shear. The shear field can be produced by any Galactic sub-structures such as globular clusters and the Galactic bulge. Here, we only consider the Galactic bulge and globular clusters as typical examples of the shear, and model their mass distribution as a point mass or the Plummer's model. The Galactic bulge is significantly extended along the line of sight and, therefore, the mass distribution has to be weighted by the factor $(D_l D_{l's})/D_s$ and projected along the line of sight; the bulge mass distribution located near the source plane contributes little while those near the half of the distance to the source contributes most. But in this work we model the bulge as a planar mass distribution at the same distance as that of the lensing star for simplicity.

1. Point mass: When the lensed images are located far from the source of the shear, the shear field may be approximated by that produced by a point mass. When the mass distribution consists of a lens with mass m located at the origin of the coordinate and an additional mass with mass M located at \mathbf{r}_1 (in units of r_E), the (additional) deflection potential $\psi(\mathbf{r})$ in equation (12) becomes

$$\psi(\mathbf{r}) = \frac{M}{m} \ln |\mathbf{r} - \mathbf{r}_1|. \quad (39)$$

Shear γ and convergence κ are calculated from equation (15):

$$\gamma = \frac{M}{m} \frac{1}{R^2}, \quad \kappa = 0. \quad (40)$$

Convergence disappears ($\kappa = 0$) because the beam is empty, and the reduced shear is equal to the shear, $\tilde{\gamma} = \gamma$.

2. Plummer’s model: As an example of extended mass distribution, we choose the Plummer’s model that approximates the surface mass distribution of a globular cluster (Plummer 1915; Binney & Tremaine 1987). In the Plummer’s model, the surface mass density is expressed as

$$\Sigma(\mathbf{r}) = \frac{M}{\pi r_0^2} \frac{1}{[1 + (r/r_0)^2]^2}, \quad (41)$$

where M is the total mass and r_0 is the core length in units of r_E . The radius r_h containing half the total mass is equal to $1.3048r_0$. Then, the deflection potential $\psi(\mathbf{r})$ due to the Plummer’s mass distribution centered at \mathbf{r}_1 becomes

$$\begin{aligned} \psi(\mathbf{r}) &= \frac{1}{\pi} \int_{R^2} d^2r' \frac{\Sigma(\mathbf{r}' - \mathbf{r}_1)}{\Sigma_{cr}} \ln |\mathbf{r} - \mathbf{r}'| \\ &= \frac{M}{m} \ln[(\mathbf{r} - \mathbf{r}_1)^2 + r_0^2]^{1/2}. \end{aligned} \quad (42)$$

Again, γ and κ are calculated from equation (15):

$$\gamma = \frac{M}{m} \frac{r_1^2}{(r_1^2 + r_0^2)^2} \quad (43)$$

and

$$\kappa = \frac{M}{m} \frac{r_0^2}{(r_1^2 + r_0^2)^2}. \quad (44)$$

Unlike the point mass case, the convergence κ is not zero because there is mass within the beam.

Figure 9a shows the values of $\tilde{\gamma}$ and κ as functions of the distance from the center of the mass distribution when the shear is produced by the Galactic bulge with a total mass of $M = 1.3 \times 10^{10} M_\odot$ and located at 8.5 kpc from the Earth. We assume that the lens star of $1M_\odot$ is also located at 8.5 kpc and the source star at 9.5 kpc. Solid curve represents $\tilde{\gamma}$ when the bulge is modeled as a point mass while dotted curve as the Plummer’s model with $r_0 = 500$ pc. Dashed curve shows κ for the Plummer’s model. Figure 9b is the same as Figure 9a for a $10^6 M_\odot$ globular cluster at 4 kpc with $r_0 = 2$ pc, $1 M_\odot$ lens star at the same 4 kpc, and a source star at 8.5 kpc. Hence, we expect the shear $\tilde{\gamma}$ produced by typical globular clusters or the Galactic bulge to be in the range of $10^{-6} \sim 10^{-4}$.

Shown in Figure 10a is the maximum distortion of the centroid shift in arcseconds when a microlensing event occurs in the Galactic bulge. If future astrometric observation can achieve the positional accuracy down to ~ 1 micro-arcsec, then $\tilde{\gamma} \sim 10^{-5.5}$ shear field can

be detected in very high magnification events with $u_0 \leq 0.002$. When a microlensing event occurs near a globular cluster (Fig. 10b), $\tilde{\gamma} \sim 10^{-4.5}$ shear field can be detected for events with $u_0 \leq 0.05$. On the other hand, in order to detect the deviation of a typical light curve for $\tilde{\gamma} = 10^{-5.5}$ and $u_0 = 0.01$, photometric accuracy should be better than $\Delta m \leq 10^{-3.5}$.

Although we may be able to measure the shear in microlensing events, the measurement alone does not tell us about the source of the shear. The shear may be from the Galactic sub-structures, but it can also be from many other objects. The most obvious source is the binary companion. A binary companion at a typical distance of ~ 35 AU (Duquennoy & Mayor 1991) will produce a shear close to 10^{-3} , two to three orders of magnitude larger than the shear by the Galactic bulge. The distribution of the binary period and the mass ratio (Duquennoy & Mayor 1991) implies 85% of all binary companions will produce $\gamma \geq 10^{-6}$. So the shear due to binary companion will dominate or be comparable to the shear expected from Galactic sub-structures. The shear can be also produced by planetary companions. Planets detected in the current microlensing experiments produce shear in the range $\tilde{\gamma} \sim 10^{-3} - 10^{-5}$. A typical Earth-mass planet at a distance of $\sim 2R_E$ ($R_E \simeq 4$ AU for $1 M_\odot$) from the lens produces $\tilde{\gamma} \sim 10^{-6}$, while Pluto-mass planet at a distance $\sim 10R_E$ produces $\tilde{\gamma} \sim 10^{-10}$. Projected companion stars, unassociated but located near the lensing star in the projected sky, will also affect lensing similarly. Hence, in practice it will be difficult to identify the shear by Galactic sub-structures against the shear by companion stars. Still, there can be some microlensing events that are not affected by companion star or in which the shear by Galactic sub-structure may be measured from the statistical analysis of many events as in cosmological weak lensing systems.

There may also be cases for which we may set an upper limit on the value of the shear. A very small upper limit on shear suggests the non-existence of a binary companion or a Galactic structure. For example, if we measure $\gamma < 10^{-7.2}$, we can expect that the lens does not have a companion with more than 95% confidence if we assume the distribution of the binary companion by Duquennoy & Mayor (1991).

Complications in usual microlensing events, for example, blending and binary source, will also affect microlensing under shear. For example, blending decreases the deviation in the image centroid shift and the light curve (Fig. 11b as compared to Fig. 11a) and the binary source completely messes up the centroid shift trajectory (Fig. 11c). However, since the shape of the trajectory mainly depends on the size of the shear, fitting the full trajectory may sort out these complications.

Although the typical shear expected from the Galactic bulge or globular clusters is too small or the clear case that enables the determination of shear is too infrequent to be comfortably detected by current or near-future microlensing experiments, next generation

microlensing experiments may enable us to measure the magnitude and the direction of even smaller shear fields among numerous microlensing events. Then, from the theoretical framework of weak lensing, the shear map can be inverted to reproduce the mass distribution (see e.g., Mellier 1999; Bartelmann & Schneider 2001; Refregier 2003), making it possible to map or at least constrain the Galactic mass distribution. Since all our discussions are based on normalized units, the reproduced mass distribution will be in units of Σ_{cr} per θ_E^2 . If D_s and D_l are additionally determined, the mass distribution can be determined in physical units.

5. Summary

We investigated microlensing under a shear, which might be produced by Galactic substructures such as globular clusters or the Galactic bulge. We analyzed its effect on the microlensing light curves and astrometric centroid shift trajectories. We found the followings:

1. The light curve deviation from the Paczyński curve increases as the shear increases and the impact parameter decreases. The positions and heights of the maximum deviation vary depending on the direction of the source trajectory: the light curve becomes asymmetric if the source trajectory is not parallel or perpendicular to the shear direction.

2. The centroid shift trajectory in the presence of shear deviates from a simple ellipse, especially when the source is within the Einstein ring. The magnitude of the maximum distortion depends on shear and its direction, and becomes largest when the trajectory is parallel or perpendicular to the shear direction. The time of maximum distortion is nearly independent of the impact parameter. The distortion of the centroid shift trajectory increases as the impact parameter decreases and the shape becomes very complex when the impact parameter is very small.

3. If we measure the distortion of the astrometric centroid shift trajectory and the time of the maximum distortion, we can determine the shear and its direction.

4. The magnitude of the shear produced by the Galactic bulge or globular clusters near the Galactic center is of the order of 10^{-6} to 10^{-4} in normalized units. This shear, in principle, could be detected by future microlensing experiments, especially in high magnification events.

Successful measurement of the shear in various directions in the Galaxy with next generation microlensing experiments may eventually lead to the mapping of the Galactic mass distribution.

We thank the referee, Scott Gaudi, for many insightful comments, which have improved the paper greatly. We also thank Dong Wook Lee and Cheongho Han for careful reading of the manuscript. This work is the result of research activities Astrophysical Research Center for the Structure and Evolution of the Cosmos (ARCSEC) supported by the Korea Science & Engineering Foundation (KOSEF).

REFERENCES

- Alcock C. et al., 1993, *Nature*, 365, 621
- An J. H., 2005, *MNRAS*, 356, 1409
- An J. H., & Evans N. W., 2006, *MNRAS*, 369, 317
- Aubourg E. et al., 1993, *Nature*, 365, 623
- Bartelmann M., & Schneider P., 2001, *Phys. Rep.*, 340, 291
- Binney J., & Tremaine S., 1987, *Galactic Dynamics*, Princeton, New Jersey
- Chang K., & Refsdal S., 1979, *Nature*, 282, 561
- Chang K., & Refsdal S., 1984, *A&A*, 132, 168
- Dominik M., 1999a, *A&A*, 341, 943
- Dominik M., 1999b, *A&A*, 349, 108
- Duquennoy A., & Mayor M., 1991, *A&A*, 248, 485
- Fischer D. A., & Marcy G. W., 1992, *ApJ*, 396, 178
- Gott, J. R. III, *ApJ*, 243, 140
- Gould A., 2000, *ApJ*, 542, 785
- Han C., Chun M. S., & Chang K., 1999, *ApJ*, 526, 405
- Han C., & Park M., 2001, *JKAS*, 34, 81
- Han C., 2002, *MNRAS*, 329, 163
- Han C. et al., 2005, *ApJ*, 618, 972

- Jeong Y., Han C., & Park S. H., 1999, *ApJ*, 551, 569
- Kovner I., 1987, *ApJ*, 312, 22
- Mellier Y., 1999, *ARA&A*, 37, 127
- Paczynski B., 1986, *ApJ*, 304, 1
- Plummer H. C., 1915, *MNRAS*, 76, 107
- Refregier A., 2003, *ARA&A*, 41, 645
- Schneider P., Ehlers J., & Falco E. E., 1992, *Gravitational Lensing*, Springer, Berlin
- Udalski A. et al., 1992, *Acta Astron.*, 42, 253
- Walker M. A., 1995, *ApJ*, 453, 37

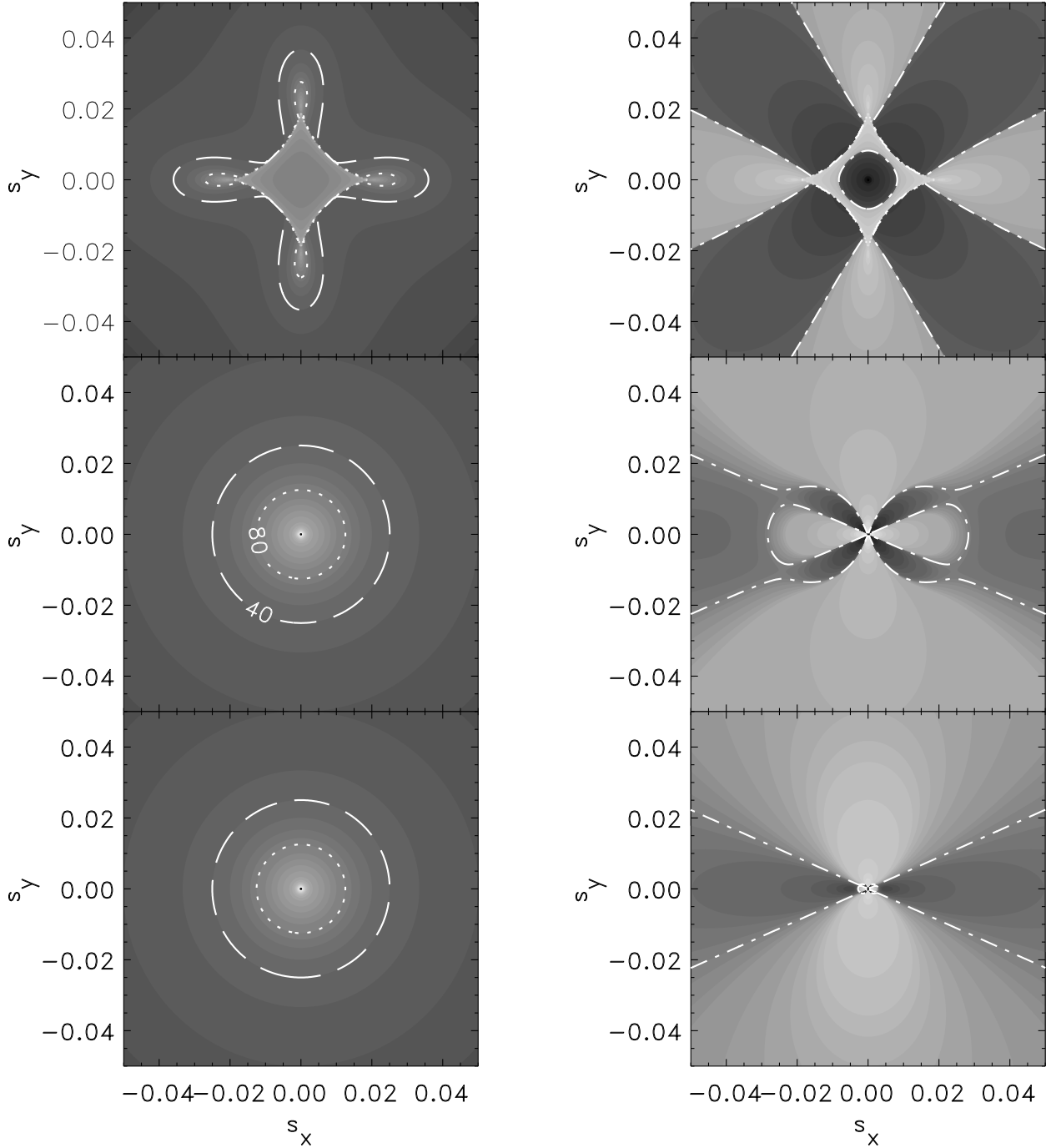


Fig. 1.— Magnification map. Grayscale maps of the magnification A_γ (left panel) and the excess magnification δA (right panel) as a function of source position (s_x, s_y) for reduced shear $\tilde{\gamma} = 10^{-2}$ (top), 10^{-4} (middle), and 10^{-6} (bottom). Contours in the left panels represent $A_\gamma = 40$ (long dashed curve) and $A_\gamma = 80$ (dotted curve). Gray scale in the right panels represents positive (bright) and negative (dark) deviation regions and dot-dashed curve shows $\delta A = 0$ regions.

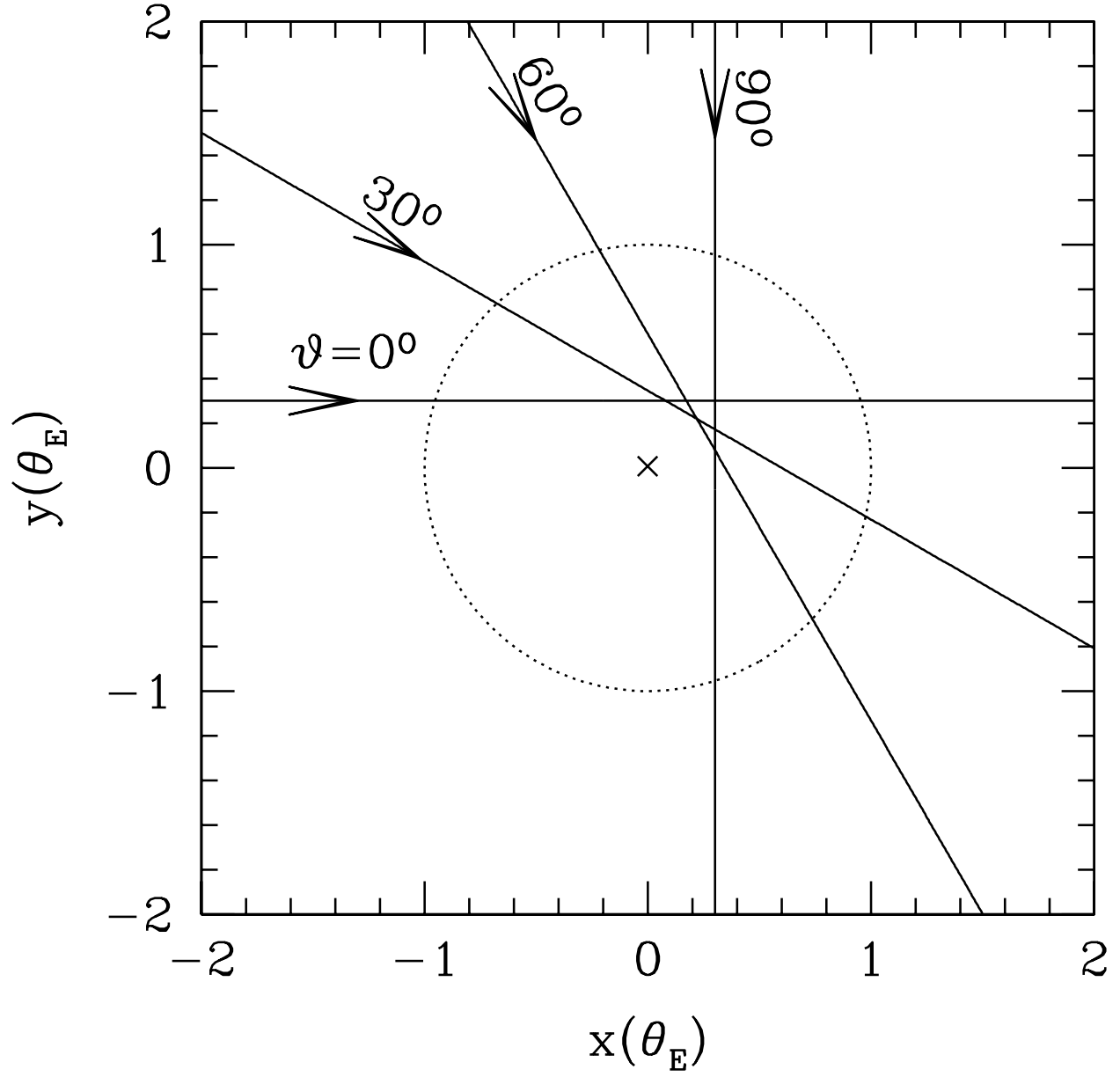


Fig. 2.— Geometry of lensing. The straight lines with an arrow represent source trajectories with different ϑ . We define ϑ as the angle between the x -axis and the source trajectory. All source trajectories have the same impact parameter $u_0 = 0.3$. The dotted ring around the lens, marked by ‘x’, shows the Einstein ring.

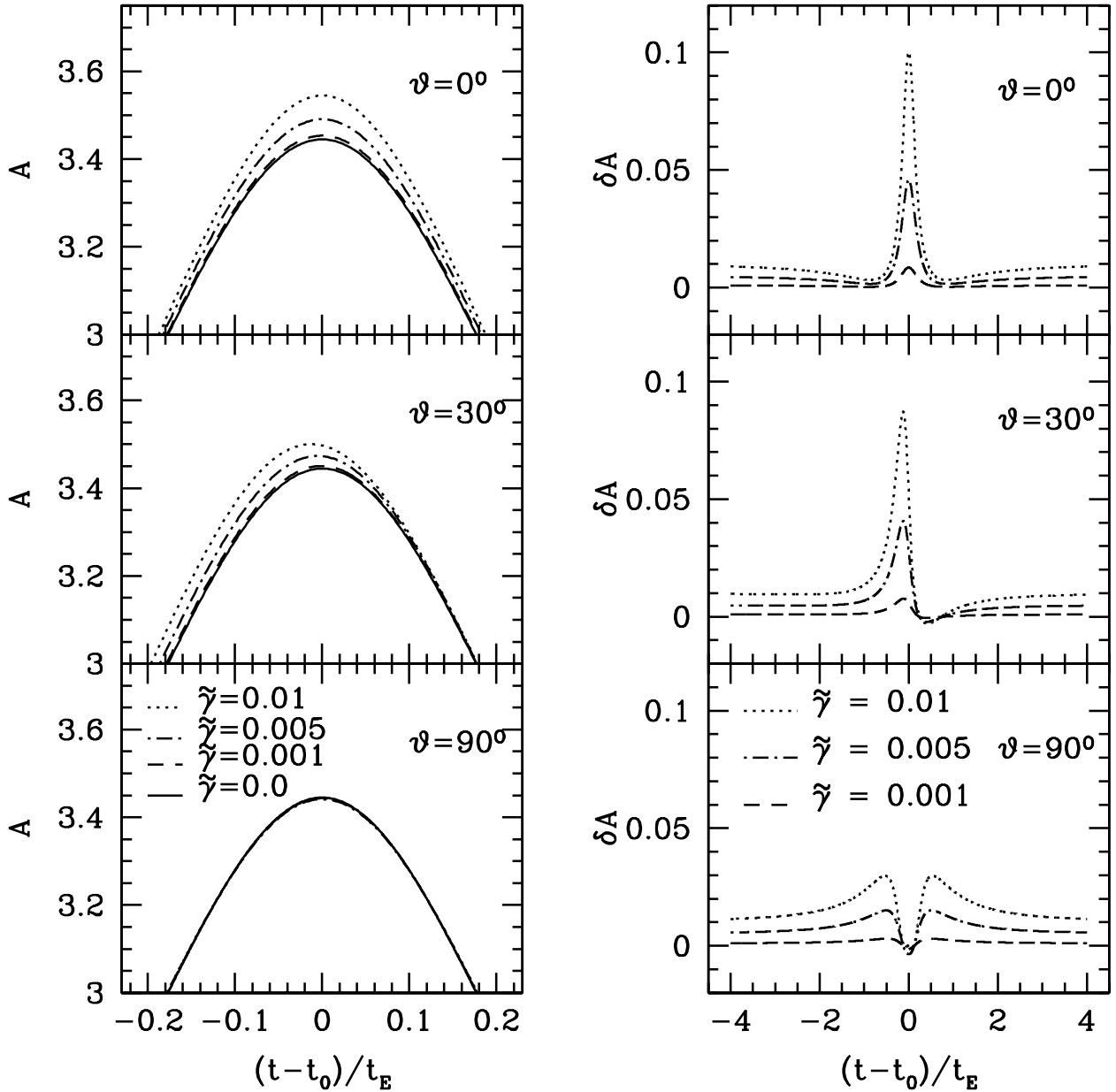


Fig. 3.— Light curves and the excess magnifications. The left panels show the light curves for the source trajectories ($u_0 = 0.3$) in Figure 1 with the shear value of $\tilde{\gamma} = 0.01, 0.005, 0.001$. All curves show the magnification near the peak, and the solid curves are the magnification without shear ($\tilde{\gamma} = 0.0$). The right panels show the difference in magnification between the light curve in the presence of shear and that in the absence of shear as a function of time for three different source trajectories.

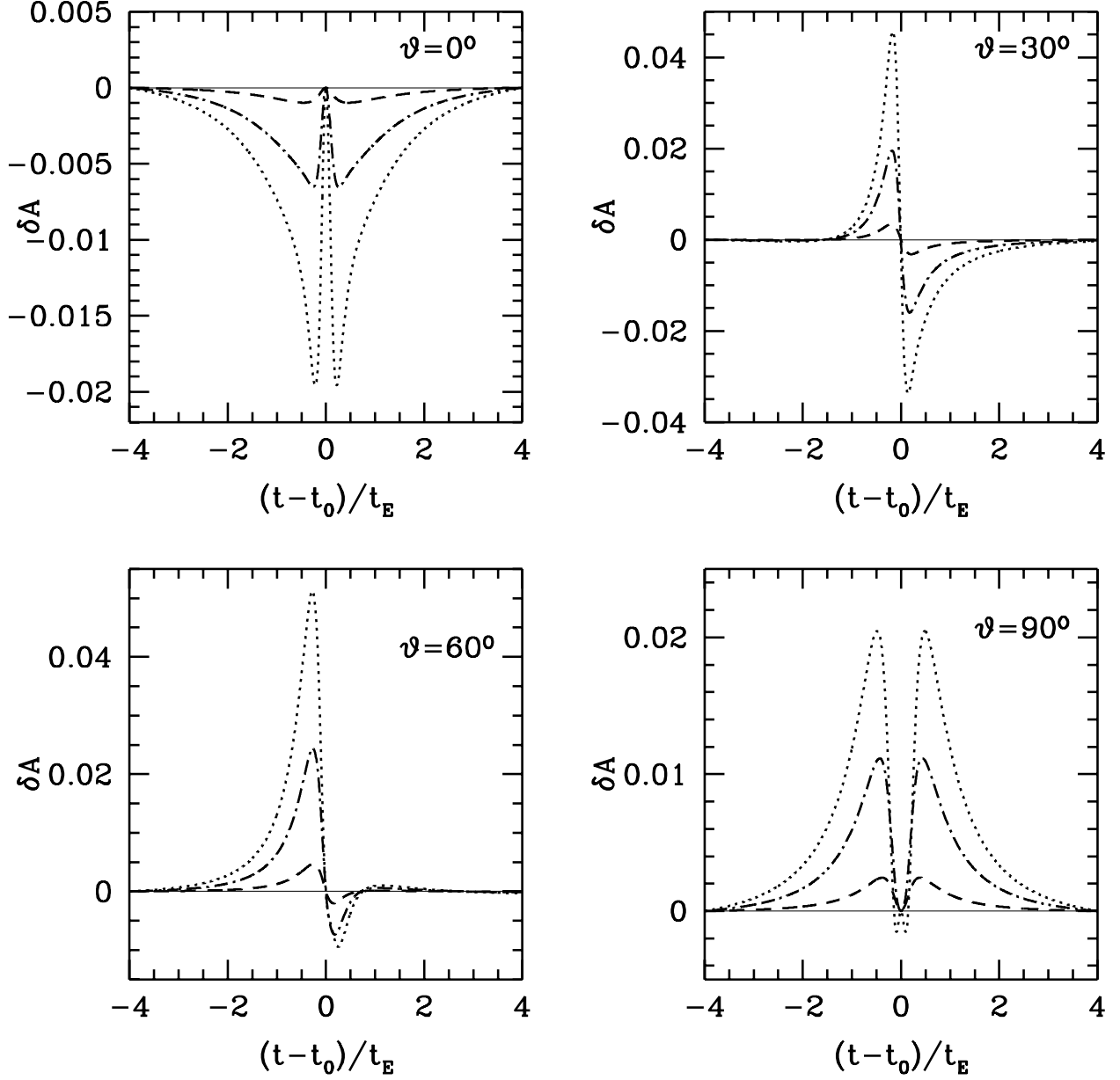


Fig. 4.— Deviation in the light curves. Difference between the light curve with shear and the corresponding Paczyński curve as a function of time for different source trajectories. Lines are for the same $\tilde{\gamma}/s$ in Figure 3.

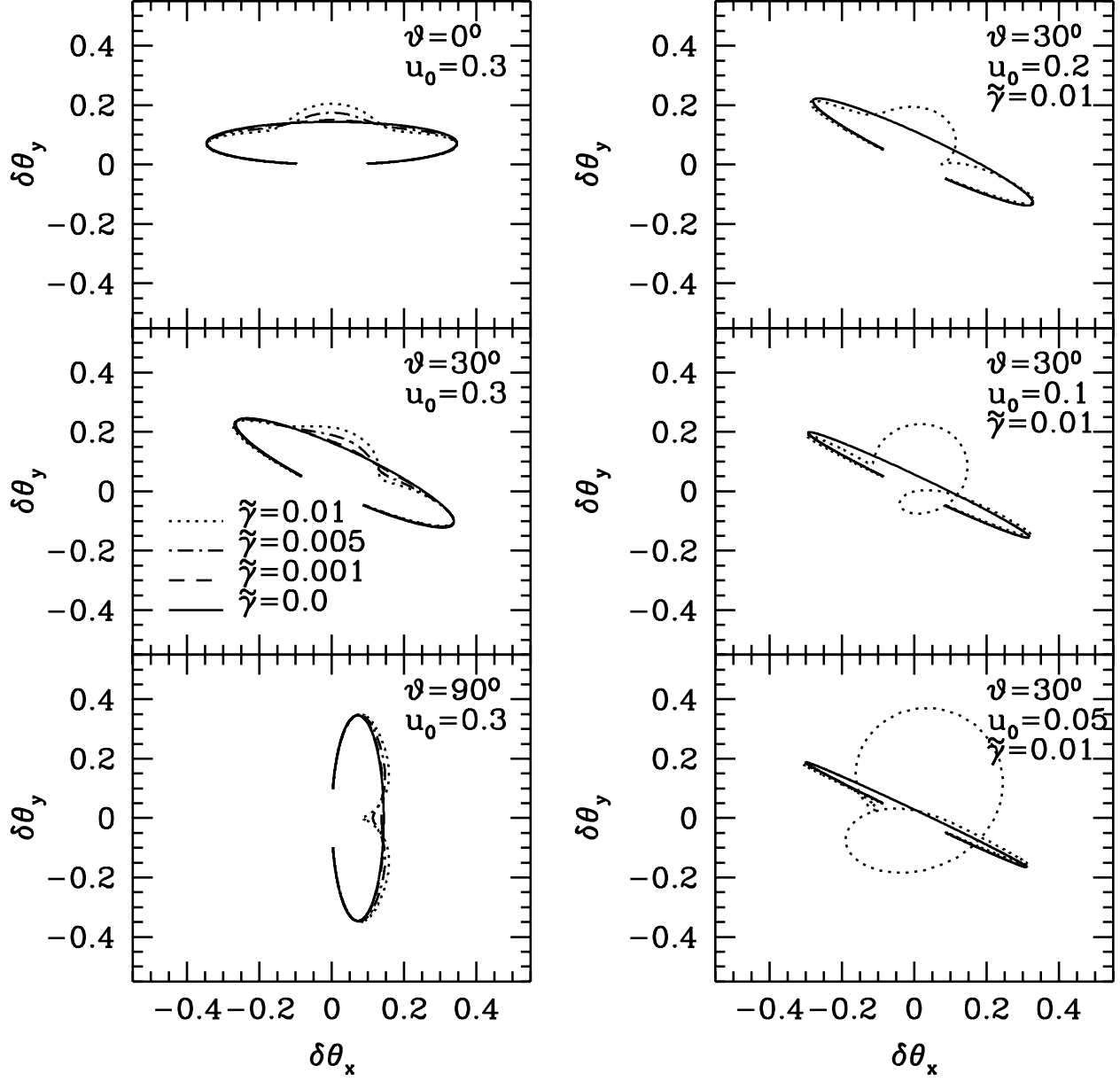


Fig. 5.— Centroid shift trajectories. The left panels show the change of centroid shift trajectories in units of θ_E for different angle ϑ and shear γ , while the right panels show the variation of centroid shift trajectories for different impact parameter u_0 . The solid curves represent the simple astrometric ellipses.

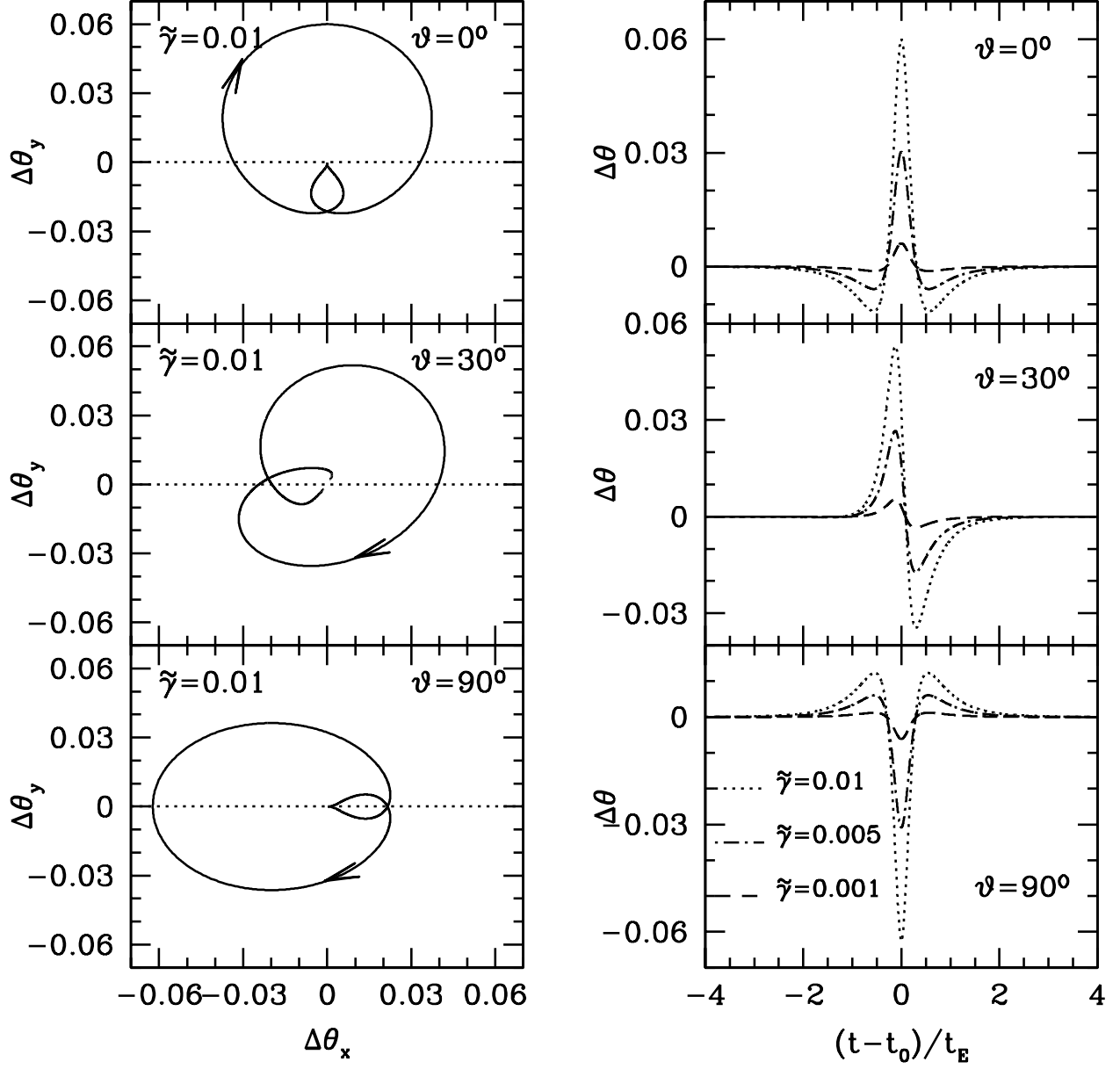


Fig. 6.— The trajectories and magnitudes of excess centroid shifts. The left panels show the trajectories of excess centroid shifts of the events for $\tilde{\gamma} = 0.01$ cases in the left panels of Figure 5. The arrow mark shows the direction of event progress. The right panels show the magnitudes of excess centroid shifts in the left panels as a function of time with three different values of shear, $\tilde{\gamma} = 0.01, 0.005, 0.001$.

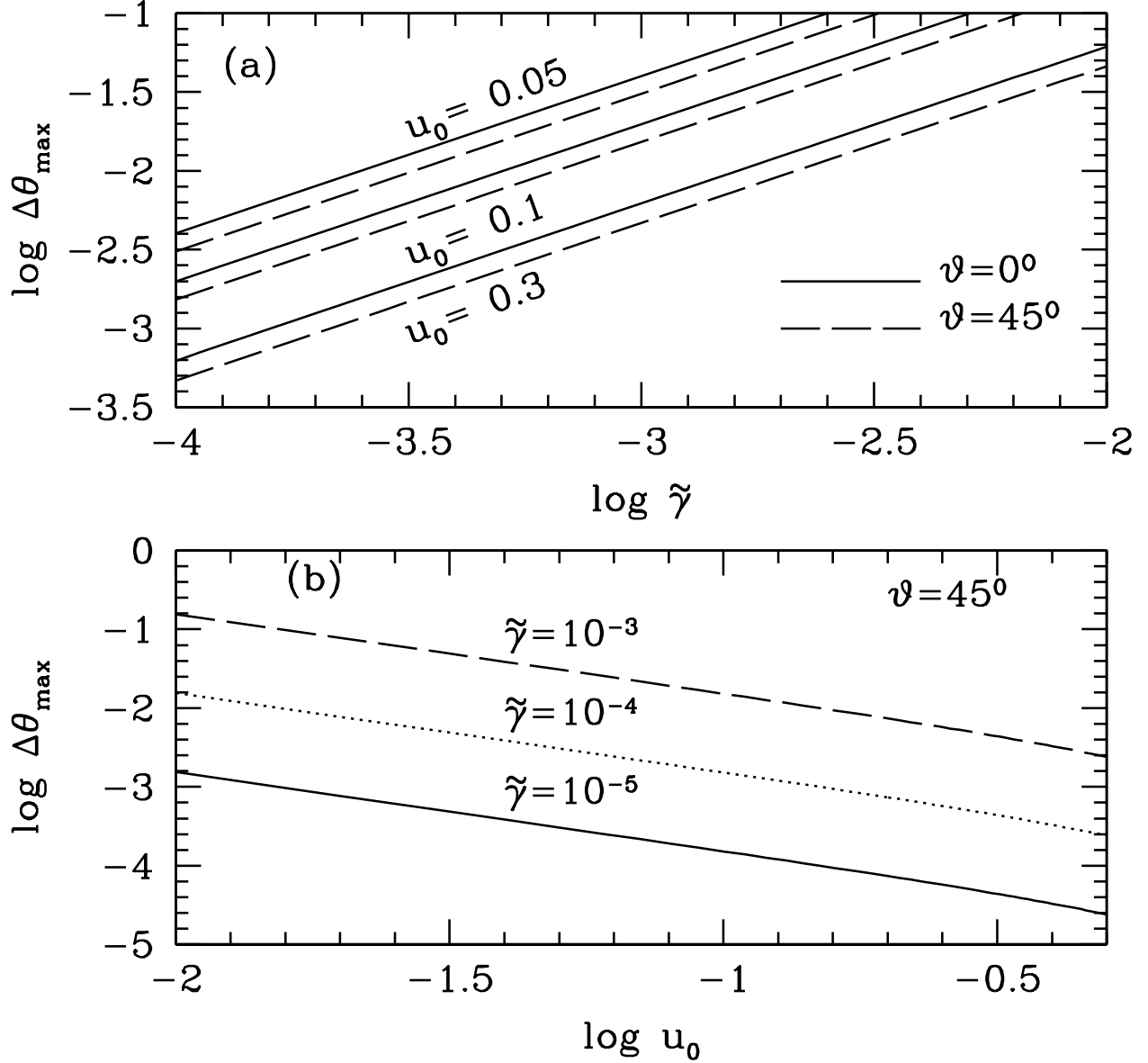


Fig. 7.— The maximum distortion of excess centroid shift. (a) The maximum distortion of excess centroid shift $\Delta\theta_{max}$ for different values of u_0 and ϑ as a function of shear $\tilde{\gamma}$. We show $\Delta\theta_{max}$ for $\vartheta = 0^\circ$ and 45° only because other source trajectories appear between the two cases. (b) The maximum distortion $\Delta\theta_{max}$ as a function of u_0 for different values of $\tilde{\gamma}$ and $\vartheta = 45^\circ$.

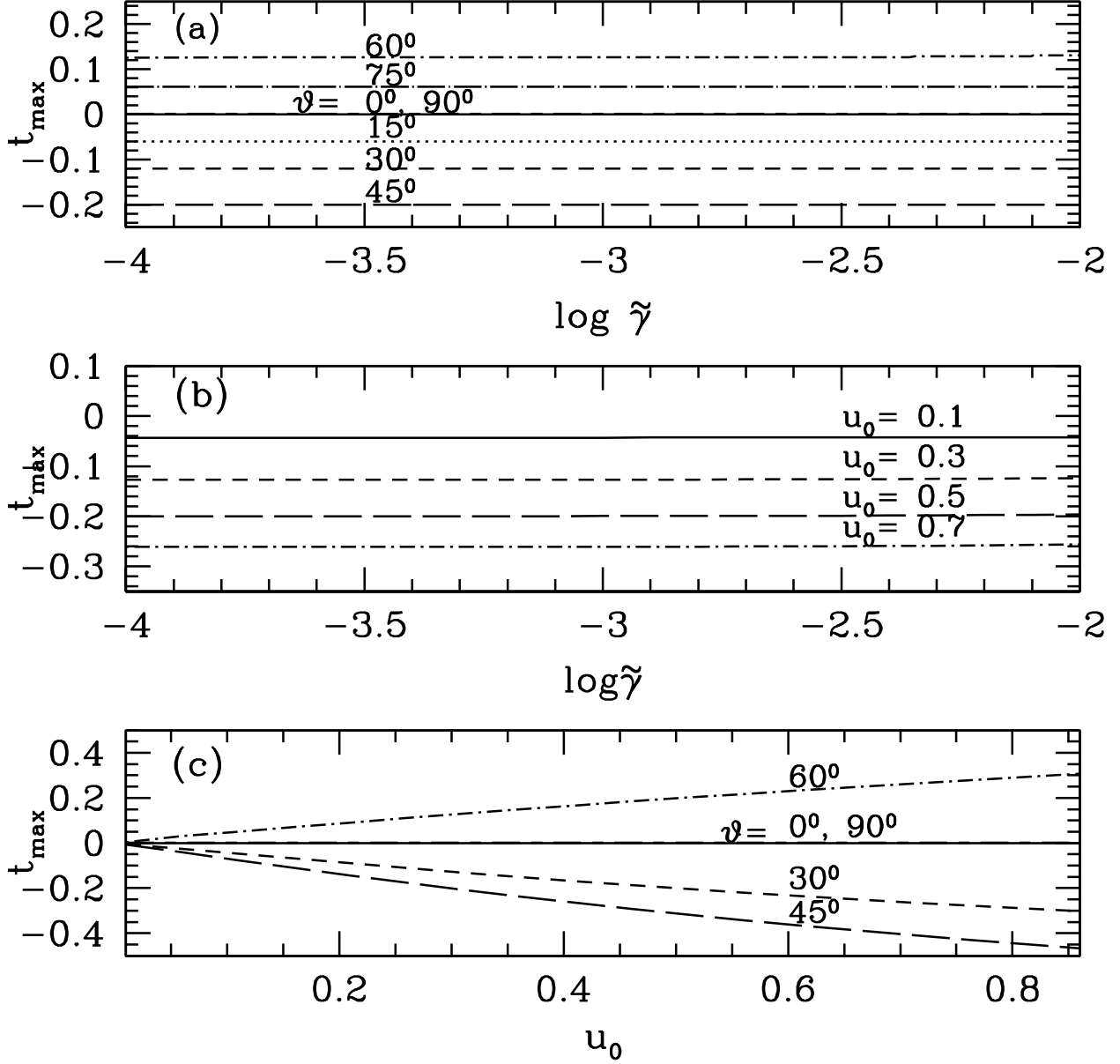


Fig. 8.— The time of maximum astrometric distortion. The time of maximum distortion of excess centroid shift, t_{\max} , as a function of $\tilde{\gamma}$ and u_0 : (a) for fixed $u_0 = 0.3$, (b) for fixed $\vartheta = 30^\circ$ and (c) for fixed $\tilde{\gamma} = 10^{-3}$.

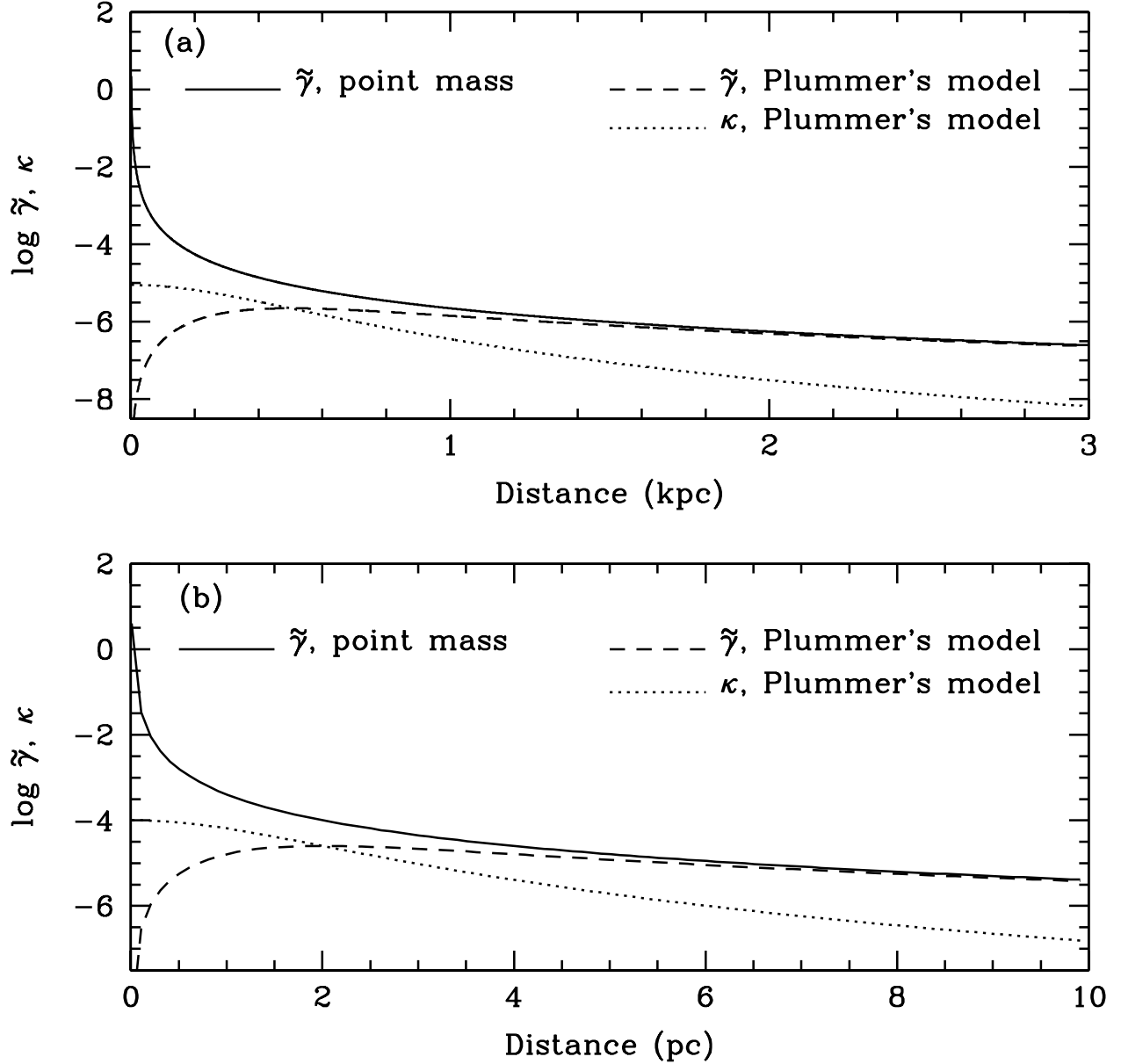


Fig. 9.— Shear and convergence from the Galactic sub-structures. (a) Shear $\tilde{\gamma}$ and convergence κ as functions of the distance from the center of the mass distribution for $1.3 \times 10^{10} M_{\odot}$ Galactic bulge at 8.5 kpc for $1 M_{\odot}$ lens at 8.5 kpc and a source star at 9.5 kpc. Solid curve shows the value of $\tilde{\gamma}$ when the bulge is modeled as a point mass while dotted curve as a Plummer's model with $r_0 = 500$ pc. Dashed curve shows κ for Plummer's model. (b) The same for a $10^6 M_{\odot}$ globular cluster at 4 kpc with $r_0 = 2$ pc and a source star at 8.5 kpc.

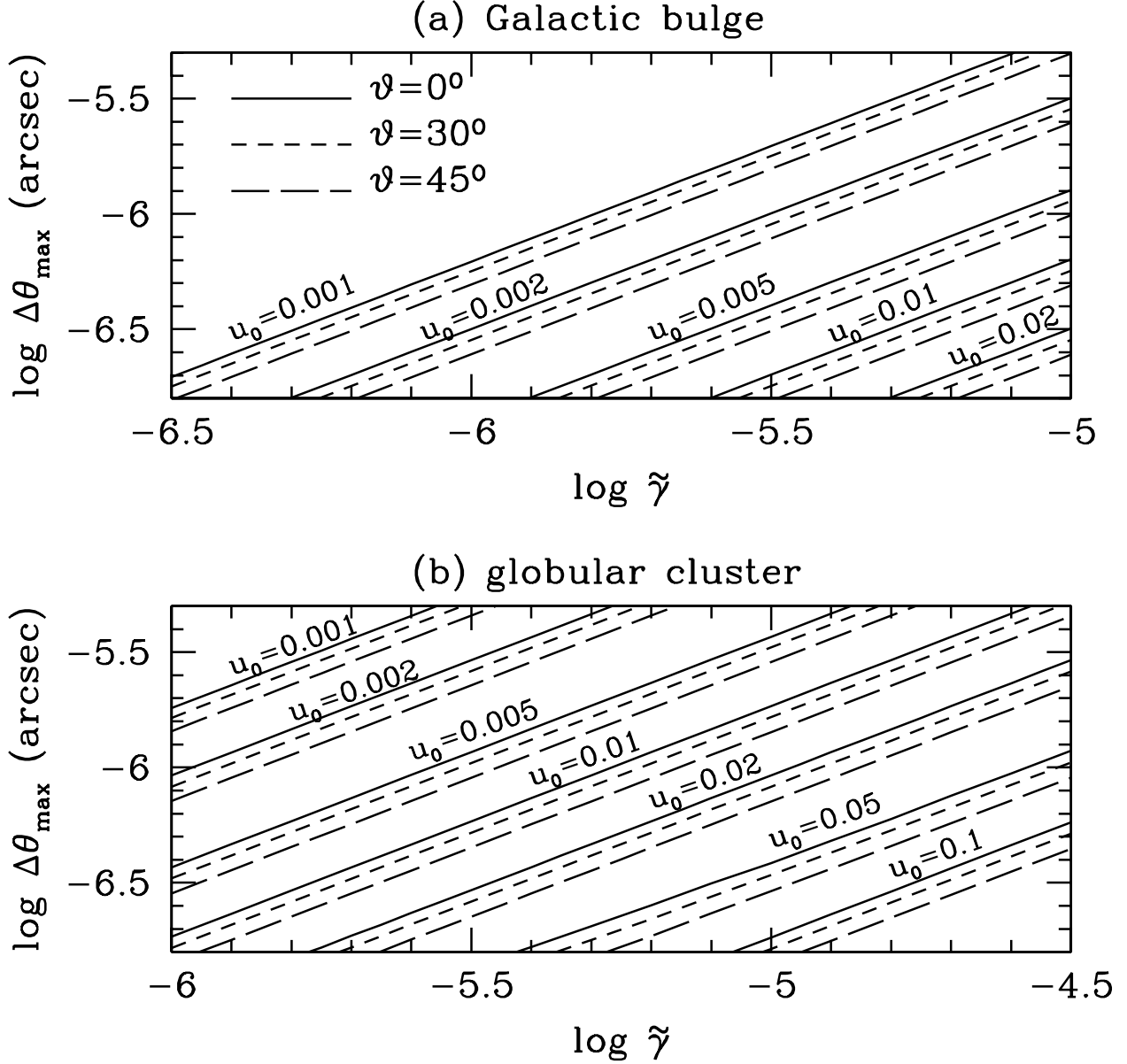


Fig. 10.— The maximum astrometric distortion expected. The maximum distortion $\Delta\theta_{\max}$ in arcseconds in excess centroid shift as a function of the shear $\tilde{\gamma}$ due to (a) the Galactic bulge ($D_s = 9.5$ kpc, $D_l = 8.5$ kpc) and (b) a globular cluster ($D_s = 8.5$ kpc, $D_l = 4.0$ kpc), both with a $1 M_\odot$ lens. Solid lines are for $\vartheta = 0^\circ$, dashed ones for $\vartheta = 30^\circ$, and long dashed ones for $\vartheta = 45^\circ$.

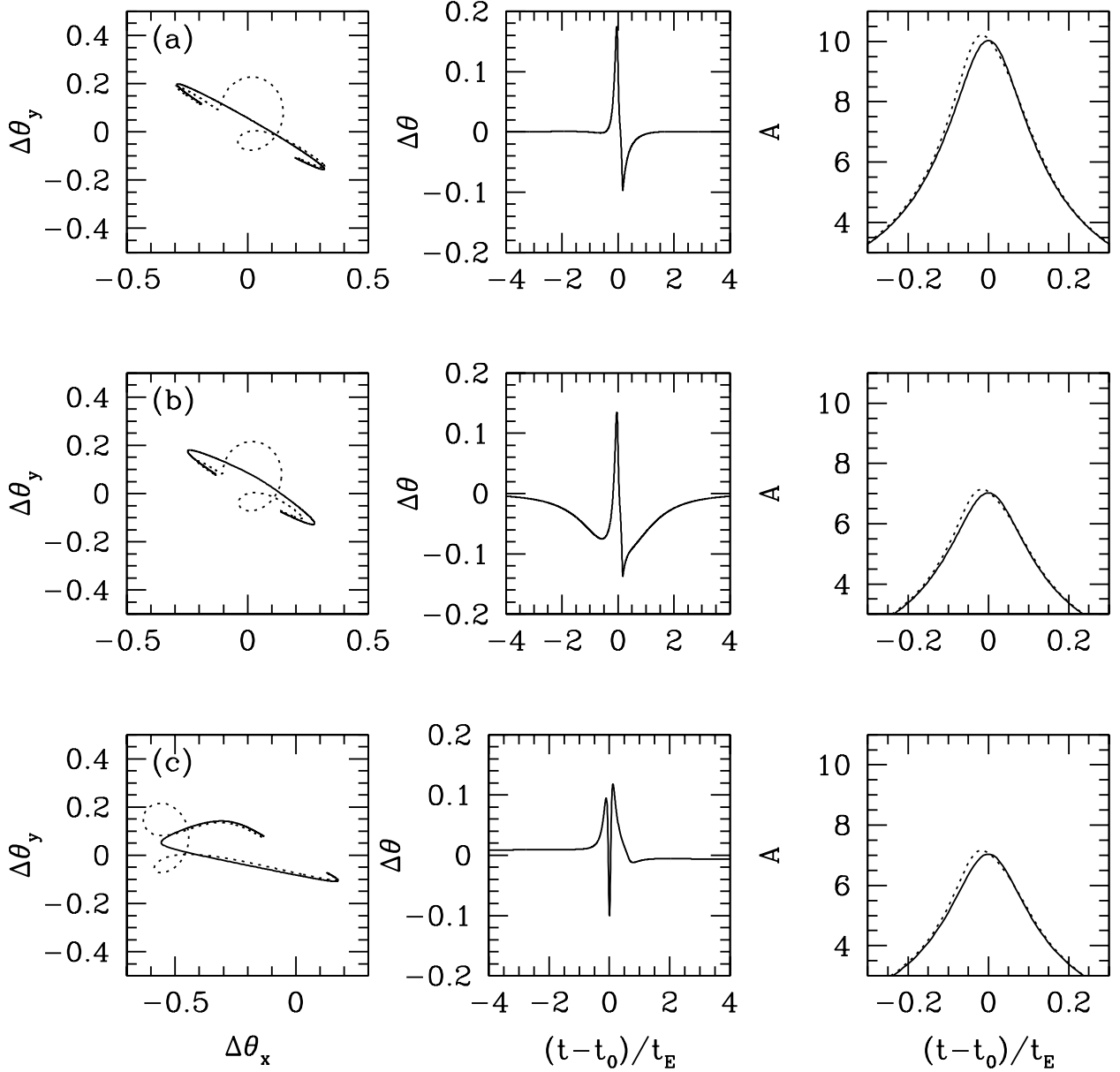


Fig. 11.— Complications in the centroid shift trajectory and the light curve from blending. The centroid shift trajectories (left), centroid shift deviations (middle), and light curves (right) are presented in case of (a) no blending (top), (b) bright lens (middle), and (c) binary source (bottom). The light fraction of the blending source is 0.5 for the lensing parameters $u_0 = 0.1$, $\vartheta = 30^\circ$, and $\tilde{\gamma} = 0.01$.